Topological antiferromagnetic semimetal for spintronics: A case study of a layered square-net system EuZnSb₂

Niraj Aryal [1,*] Qiang Li [1,2] A. M. Tsvelik [1] and Weiguo Yin [1,†]

[1]*Condensed Matter Physics and Materials Science Division, Brookhaven National Laboratory, Upton, New York 11973, USA*
[2]*Department of Physics, Stony Brook University, Stony Brook, New York 11794, USA*

We use the first-principles and effective Hamiltonian methods to study the electronic structure and magnetic properties of a recently synthesized layered antiferromagnetic square-net topological semimetal EuZnSb₂ [Phys. Rev. Res. **2**, 033462 (2020)]. The main message of the paper is that effects of small changes in the band structure produced by the magnetic ordering and changes in the orientation of the Néel vector are amplified in such transport properties as the spin Hall conductivity. We predict that the effects of the broken symmetry introduced by the ordering of the Néel vector, being very weak in the bulk, are pronounced in the surface electronic dispersion, suggesting that surface probes may be more suited to measure them. The coexistence of the magnetism with many other competing phases make this material interesting and possibly useful for quantum spintronics applications.

I. INTRODUCTION

Interplay of the topological bands and competing magnetic orders could result in novel physical properties such as large anomalous Hall effect [1] and axion electrodynamics [2]. It also presents a possibility to use magnetic reordering to manipulate electronic transport [3]. The recent discoveries of magnetic topological insulators [4] and magnetic Dirac [5–7] and Weyl [8–11] semimetals have triggered a flurry of research activities on this topic [12]. In particular, antiferromagnetic (AFM) systems with broken parity ($\mathcal{P}$) and time reversal ($\mathcal{T}$) symmetries but unbroken $\mathcal{PT}$ symmetry have attracted a lot of interests recently for novel effects such as the electrical control of AFM magnetization [13,14] and the Dirac band topology [15,16].

After Young and Kane proposed the existence of topological nodal fermions in square-net motifs [17], different variants of the square-net topological materials have been studied extensively [18,19]. Recently, antiferromagnetic semimetals consisting of strongly correlated $4f$ electrons in the 111 family of type LnSbTe [Ln = lanthanide elements] [20,21] and 112 family of type LnMn(Bi,Sb)₂ have been reported to host a topological Fermi surface similar to the well-known ZrSiS family of materials [22–25]. It is known that when the magnetic atoms directly contribute to the formation of the conduction bands as in such transition metal antiferromagnetic Dirac semimetal (AFM-DSM) systems as CuMnAs, Mn₃Ge, etc., the magnetic ordering and, in particular, the orientation of the magnetic moments can bring subtle changes in the electronic structure and related transport properties [16,26]. Such subtle changes in the band topology and

associated transport signatures in AFM-DSM caused by changes in the orientation of the magnetic moments may be useful for spintronics applications such as low power electronics and magnetic memory devices [27,28].

An influence of magnetism on the electronic dispersion and transport is less explored in the aforementioned f-electron square-net systems, where it may also lead to interesting effects. However, the conduction bands in these systems are formed by the p_x-p_y orbitals of the (Bi, Sb) square nets weakly hybridized with the f-electron bands lying far away from the Fermi level. This makes a connection between the f-electron magnetism and the conduction bands as well as the associated transport anomalies less obvious. Given the potential advantages of f-electron systems over conventional semiconductors for spintronics applications [29,30] and the availability of rich material pool and magnetic properties obtained by varying Ln elements [31], it is important to study the systems where the itinerant electrons coexist with the localized ones.

Recently, Wang *et al.* have reported a discovery of a layered $4f$ square-net material EuZnSb₂ [32]. This material is the zintl cousin of the more famous Mn-based 112 phases. Because of the unpaired $4f$ electrons, it orders antiferromagnetically with a Néel temperature (T_N) of 20 K. Density functional theory calculations showed the presence of the extended Fermi surface formed by the p electrons. In this paper we study in detail the electronic structure of various AFM phases of this material. We aim to establish if and how the orientation of the Néel vector influences the band topology and related transport properties. We find that magnetic orderings introduce small but non-negligible corrections in the gap size across the Fermi surface which have consequences in the Berry curvature related transport properties. More importantly, we find that depending on the orientation of the Néel vector, different crystalline symmetries are broken globally. Such broken symmetries are manifested in the electronic structure and transport

*naryal@bnl.gov
†wyin@bnl.gov

properties. Our findings suggest that systems with coexisting itinerant and localized f electrons can be useful platforms for topological spintronics applications and more studies along this direction are necessary.

The organization of this paper is as follows. In Sec. II we present the details of our computational methods. In Sec. III we present our results and discuss them in detail. Finally, in Sec. IV we present our conclusion and future outlook. The derivation of the tight-binding model and the effective Kondo exchange Hamiltonian is relegated to the Appendixes.

II. COMPUTATIONAL DETAILS

The density-functional-theory (DFT) calculations were done using the WIEN2K DFT package [33]. The basis size was determined by $R_{mt}K_{max} = 7$ and the primitive Brillouin zone (BZ) was sampled with a regular $18 \times 18 \times 7$ k mesh to achieve energy convergence of 1 meV. A 10 000 k-point mesh was used for the Fermi surface calculations. Some of the calculations, especially in the paramagnetic phase, were verified using the QUANTUM ESPRESSO (QE) [34] package. The Perdew-Burke-Ernzerhof (PBE) exchange-correlation functional [35] within the generalized gradient approximation (GGA) was used in all the calculations. The GGA + U_{eff} method was used to handle the Eu $4f$ orbitals. U_{eff} of 6 eV was chosen in our calculations [36–39]; however we have also verified that the results presented here remain robust for a large range of U_{eff} values. The spin-orbit coupling (SOC) was treated in the second variation method. The spin Hall conductivity calculations were done using WANNIER90 software [40,41] by taking an 80×80 Wannierized Hamiltonian. All Eu $4d$, $4f$ orbitals and Sb $5s$, $5p$ orbitals were used in the Wannierization procedure in order to accurately reproduce the DFT bands in the energy window from -1 to 1 eV.

III. RESULTS AND DISCUSSION

A. Crystal structure

EuZnSb$_2$ is a layered square-net material in the space group $P4/nmm$ (No. 129) similar to the well-known nodal-line family of materials of ZrSiS [32]. The crystal structure of EuZnSb$_2$ is shown in Fig. 1. The unit cell consists of stacking of square lattices of Eu, Zn, and two types of Sb atoms (called Sb1 and Sb2 here) along the **c** direction in the arrangement of —Zn-Sb1-Eu-Sb2-Eu-Sb1-Zn—. Sb2 and Zn atoms form a denser ($\sqrt{2} \times \sqrt{2}$) square lattice (also known as 4^4 square lattice in the crystallographic community [42]), with two atoms in each two-dimensional (2D) square plane, whereas Sb1 and Eu atoms form a less denser square lattice with just one atom in each 2D square plane. Sb2 and Zn atoms occupy the same site when projected on the **a**-**b** plane, whereas Eu (and Sb1) atoms above and below Sb2 atoms occupy the interstitial site of the 4^4 lattice and are related by inversion (or a glide) symmetry.

B. Nonmagnetic phase and Wannier tight-binding analysis

It was shown in Ref. [32] that the lowest energy antiferromagnetic phase of EuZnSb$_2$ hosts broad band dispersion close to the Fermi level. Before investigating how the band topology
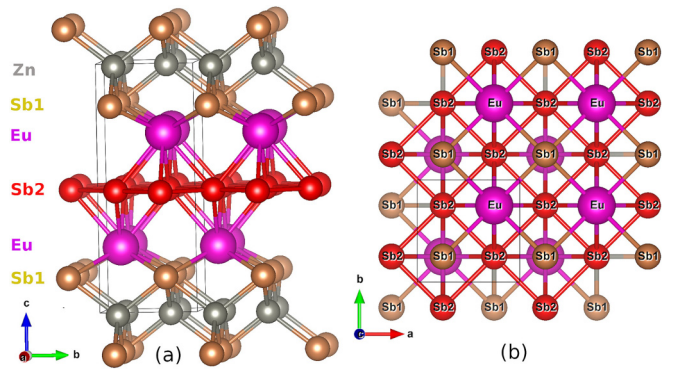

FIG. 1. The unit cell of EuZnSb$_2$. (a) The stackings of the layered square lattices along the **c** axis and (b) the projection onto the **a**-**b** plane and the denser ($\sqrt{2} \times \sqrt{2}$) square lattice of Sb2 atoms. Eu atoms above and below Sb2 atoms occupy the interstitial site of the Sb2 square lattice and are related by the glide (or inversion) symmetry; Zn atoms occupy the same site as Sb2 atoms.

changes with the change in the magnetic texture, we would like to understand the origin of the conduction bands. For this end we first study the nonmagnetic phase in the absence of the Eu-$4f$ electrons within the open core approximation to simplify the problem. Since we are interested in the electronic dispersion in the vicinity of the Fermi level, such open core electron description is approximately equivalent to the application of the Hubbard U within the mean-field approximation that pushes the localized states away from the Fermi level.

The DFT calculated band dispersion for nonmagnetic calculation in the absence of SOC are shown in Fig. 2(a) (gray lines). The band diagram shows crossings along Γ-M and Γ-X directions close to the Fermi level. Such crossings are the consequence of the band folding due to the doubling of the unit cell and are formed between the dispersive p_x-p_y orbitals from the denser square nets of Sb2 atoms. The p_z states from Sb2 atoms have smaller bandwidth and are almost completely filled. Sb1 p orbitals also contribute to the states close to the Fermi level (see band character plots in Appendix A, Fig. 10).

The red and blue dots overlapped onto the gray lines in Figs. 2(a) and 2(b) are the results from four- and six-band Wannier function descriptions, respectively, obtained by using the method of disentanglement [40]. Hopping parameters only up to the next-nearest neighbor (nnn) given in Table I are used for this comparison. The four-band model reproduces the crossings between the dispersive p_x-p_y bands along the Γ-M and X-Γ directions but it cannot describe other features in the vicinity of the Fermi level. It appears that the six-band tight-binding (TB) model is the minimal model to describe the band structure in the vicinity of the Fermi surface. Even with the nnn TB model, one can describe approximately the generic features as seen in Fig. 2(b). In fact, by including the long range hopping terms, we can reproduce all the features in the periphery of the Fermi level exactly (see Fig. 12 in Appendix A where all long range hopping matrix elements are included in the six-band model). The Wannier orbitals are formed by the bond directed p_x, p_y, and p_z-like orbitals centered on the Sb2 atoms forming the square lattice as shown in Fig. 2(c).
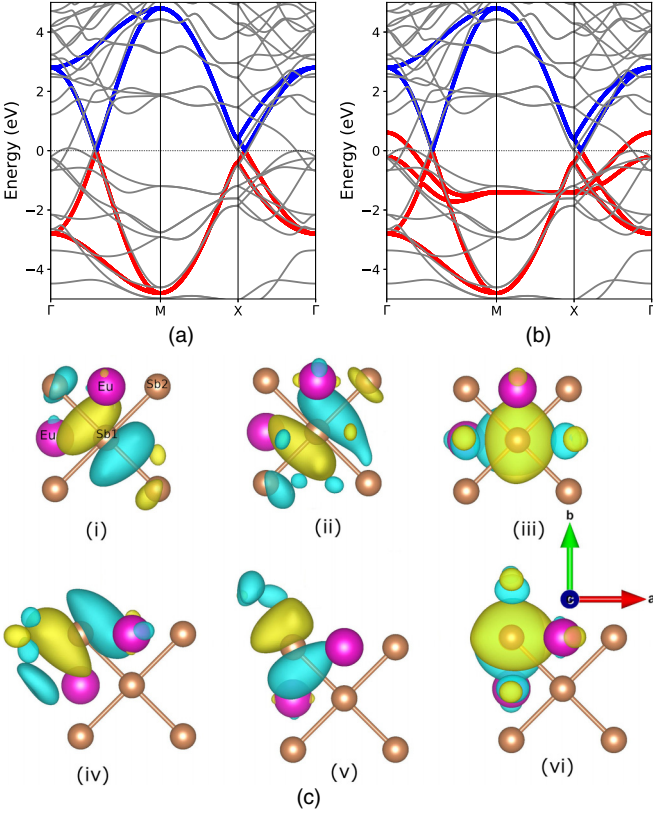
FIG. 2. Comparison between the DFT calculated bands (gray lines) with (a) four- and (b) six-band TB Hamiltonian eigenvalues (red-blue dots) for the paramagnetic phase without SOC obtained using the parameters in Table I. In (c) we show the six p_x, p_y, and p_z-like Wannier orbitals used in the description of the six-band TB Hamiltonian.

FIG. 3. Band structure from a nnn 4×4 Hamiltonian using the tight-binding parameters in Table I. (a) Sublattice and $\mathcal{R}_4$ is broken explicitly in the 4×4 model by introducing on-site anisotropy and making the σ and π hopping different along $\hat{x}$ and $\hat{y}$ direction. (b) The effect of SOC is included. The insets show the gap openings in the band crossings.

In the presence of the SOC, the entire Fermi surface gaps out. We find the form of SOC in our TB Hamiltonian to be $(\lambda \sigma_z \tau_y + \delta \gamma_z \sigma_z \tau_z)$ where λ and δ are constants and γ, σ, τ are the Pauli matrices acting on the site, spin, and orbital indices, respectively. The first term introduces coupling between the p_x and p_y orbitals of the same site and same spin, whereas the second term introduces the on-site asymmetry. Figure 3(b) shows the action of SOC on the nnn tight-binding model using $\delta = 0.1$ and $\lambda = 0.2$ which are extracted from the *ab initio* Wannier function analysis. In addition to gapping out the entire Fermi surface, the introduction of SOC breaks twofold degeneracy at the Γ point but preserves crossings at M and X points away from the Fermi level. These observations are consistent with the DFT calculation.

C. Magnetic phases and electronic structure

Having explored the electronic dispersion of the nonmagnetic phase in detail, we are now in the position to understand the influence of magnetic texture in the electronic properties. Reference [32] found that two AFM patterns (referred to as AAF and AAF3) of EuZnSb$_2$ are competing for the ground state, i.e., having very small energy differences well within the error bar of the calculations. The different magnetic patterns

Qualitatively, the four-band model Hamiltonian in the basis of the p_x and p_y orbitals is sufficient to understand the origin of the band dispersion along the Γ-M and X-Γ [43]. Hence, in the following we only discuss the simple four-band model to understand the effect of $\mathcal{R}_4$ symmetry breaking introduced by the magnetic Eu atoms and the action of the spin-orbit coupling. Notice that in the absence of the nnn term, fourfold degenerate bands are present right at the X high symmetry point, whereas the nnn term makes the bands twofold degenerate slightly away from the X point (see Fig. 11). We refer the reader to Appendix A for an exact analytical expression of the eigenvalues from the 4×4 Hamiltonian and other effective Hamiltonian analysis.

Gap on the Fermi surface: The Fermi surface (FS) can be gapped partially along Γ-M by breaking the sublattice symmetry (or equivalently inversion or glide symmetry of the 2D square plane). This can be done easily in our TB Hamiltonian by introducing the on-site anisotropy term. However, in order to open a gap at the X-Γ direction, one needs to break both sublattice and $\mathcal{R}_4$ symmetry; the latter can be introduced in our TB model by making the σ and π hoppings asymmetric along the $\hat{x}$ and $\hat{y}$ directions. Figure 3(a) presents the case of opening gaps in the band crossings by introducing such terms in our TB model.
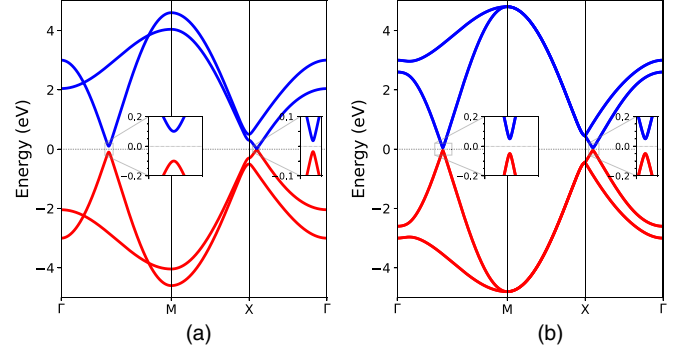
TABLE I. Tight-binding parameters (in eV) for the six-band Wannier functions in the basis of the p_x, p_y, and p_z-like Wannier orbitals centered on the Sb2 atoms forming square lattice. The nearest neighbor (nn) p_i-p_i hopping integrals are $t_\sigma = 1.9$ and $t_\pi = -0.5$ for the σ- and π-bonding-like orbital overlaps, respectively.

$\langle WFs|H|WFs \rangle$	Sb p_x	p_y	p_z
Sb ϵ-μ	0.12	0.12	-1.0
Sb$_{nn}$ p_x	t_σ; t_π	0.00	-0.05
Sb$_{nn}$ p_y	0.00	t_σ; t_π	-0.05
Sb$_{nn}$ p_z	-0.05	-0.05	-0.10
Sb$_{nnn}$ p_x	0.00	± 0.10	0.00
Sb$_{nnn}$ p_y	± 0.1	0.00	0.00
Sb$_{nnn}$ p_z	0.00	0.00	0.20

TABLE II. Calculated energy difference per formula unit in meV for different magnetic patterns (see text).

Pattern	GGA	GGA + SO	GGA + SO + U (3 eV)	GGA + SO + U (6 eV)
AAF-x	0	0	0	0
AAF-z	–	0.804	0.24	0.017
AAF3-x	–	−2.85	−0.41	1.29
AAF3-z	−6.46	−6.18	−0.53	1.35
FM	1.13	−0.53	–	3.71
NM	7297	5795	–	–

studied in this work are shown in Fig. 4. Throughout this paper, the $\hat{z}$ and $\hat{x}$ magnetic phase (alternatively called soz and sox phases in the paper) imply the direction of the Néel vector ($\vec{n}$) parallel to the [001] and [100] direction, respectively. Our DFT calculations find that the energy differences between the magnetic phases depend on the value of the Hubbard interaction U. As shown in Table II, for $U = 0$, AAF3 has lower energy, whereas as U is increased, AAF becomes lower in energy. Also, the magnetic anisotropy energy is very small, i.e., the energy differences between the $\hat{z}$ and $\hat{x}$ AFM pattern are almost the same. Note that the ferromagnetic (FM) state is also closer in energy, but the nonmagnetic (NM) phase is a very high-energy state, due to the Eu^{2+} $4f^7$ high-spin electronic configuration but with weak coupling between well-localized f electrons. The relevant information about magnetic space groups and symmetry relationships is listed in Table III.

1. AAF phase

The AFM arrangement of the two Eu atoms in the primitive unit cell located above and below the Sb2 square lattice gives the AAF phase. The two antiferromagnetically aligned Eu atoms are no longer inversion symmetric irrespective of any direction of the Néel vector. This is because inversion symmetry does not operate on the spin degree of freedom. However, because of the broken inversion ($\mathcal{P}$) and broken time reversal symmetry ($\mathcal{T}$), their product $\mathcal{PT}$ is a conserved quantity which makes the bands doubly degenerate throughout the BZ. Such a magnetic space group (MSG) falls into type-II MSG.

Unlike inversion symmetry, rotation (or screw) and mirror (or glide) symmetries act on the spin degree of freedom. Hence, depending on the orientation of the Néel vector, some of the symmetries could be broken. For example, $\hat{x}$ ($\hat{z}$) direction of the Néel vector preserves (breaks) glide symmetry $\mathcal{G}_z = \{m_{001}|\frac{1}{2}\frac{1}{2}0\}$ but breaks (preserves) twofold rotation
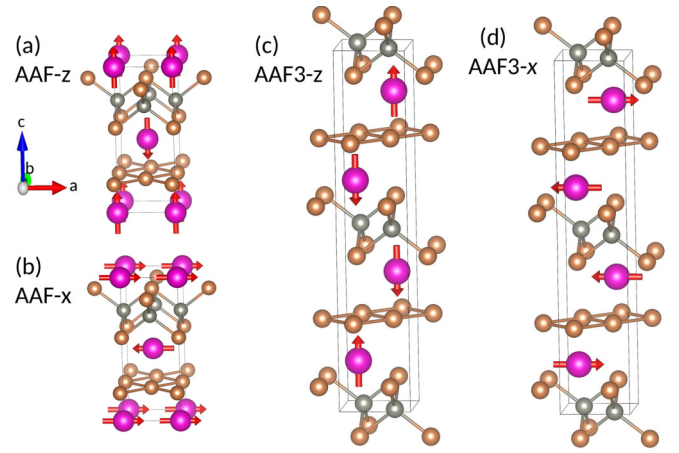
FIG. 4. (a) and (b) AAF and (c) and (d) AAF3 magnetic patterns of EuZnSb$_2$ with magnetization along the $\hat{x}$ and $\hat{z}$ axes, respectively.

symmetry $\mathcal{R}_{2z} = \{2_{001}|\frac{1}{2}\frac{1}{2}0\}$ which can be seen from the following action of the symmetry operation on the space and spin degree of freedom:

$$(x, y, z) \xrightarrow{\mathcal{G}_z} \left(x + \tfrac{1}{2}, y + \tfrac{1}{2}, -z\right),$$

$$(x, y, z) \xrightarrow{\mathcal{R}_z} \left(-x + \tfrac{1}{2}, -y + \tfrac{1}{2}, z\right),$$

$$(m_x, m_y, m_z) \xrightarrow{\mathcal{G}_z/\mathcal{R}_z} (-m_x, -m_y, m_z). \tag{1}$$

Similarly, other symmetries absent in the AAF-$\hat{x}$ magnetic phase are fourfold rotation symmetries along the **c** axis $\{4^{\pm}_{001}|\frac{1}{2}00\}$, twofold rotation along the [110] axes $\{2_{110}|\frac{1}{2}\frac{1}{2}0\}$, $\{2_{1-10}|0\}$, and the product of these symmetries with $\mathcal{PT}$ symmetry. The details of the symmetry operations present for different magnetic patterns are shown in Table III.

In the following paragraphs we will first present results from the DFT calculations which show clear differences in the bulk and surface electronic dispersion between the $\hat{z}$ and $\hat{x}$ phase. We will then derive an effective Kondo exchange Hamiltonian using parameters extracted from DFT calculations to understand some of the major findings.

a. Bulk states: The bulk band structure comparison between the AAF-$\hat{x}$ and AAF-$\hat{z}$ phases in a narrow energy window of ± 1 eV is shown in Fig. 5(a). Figure 15 in Appendix C shows the electronic dispersion and density of states (DOS) in a wider energy range. The Eu-$4f$ states are 1 eV below
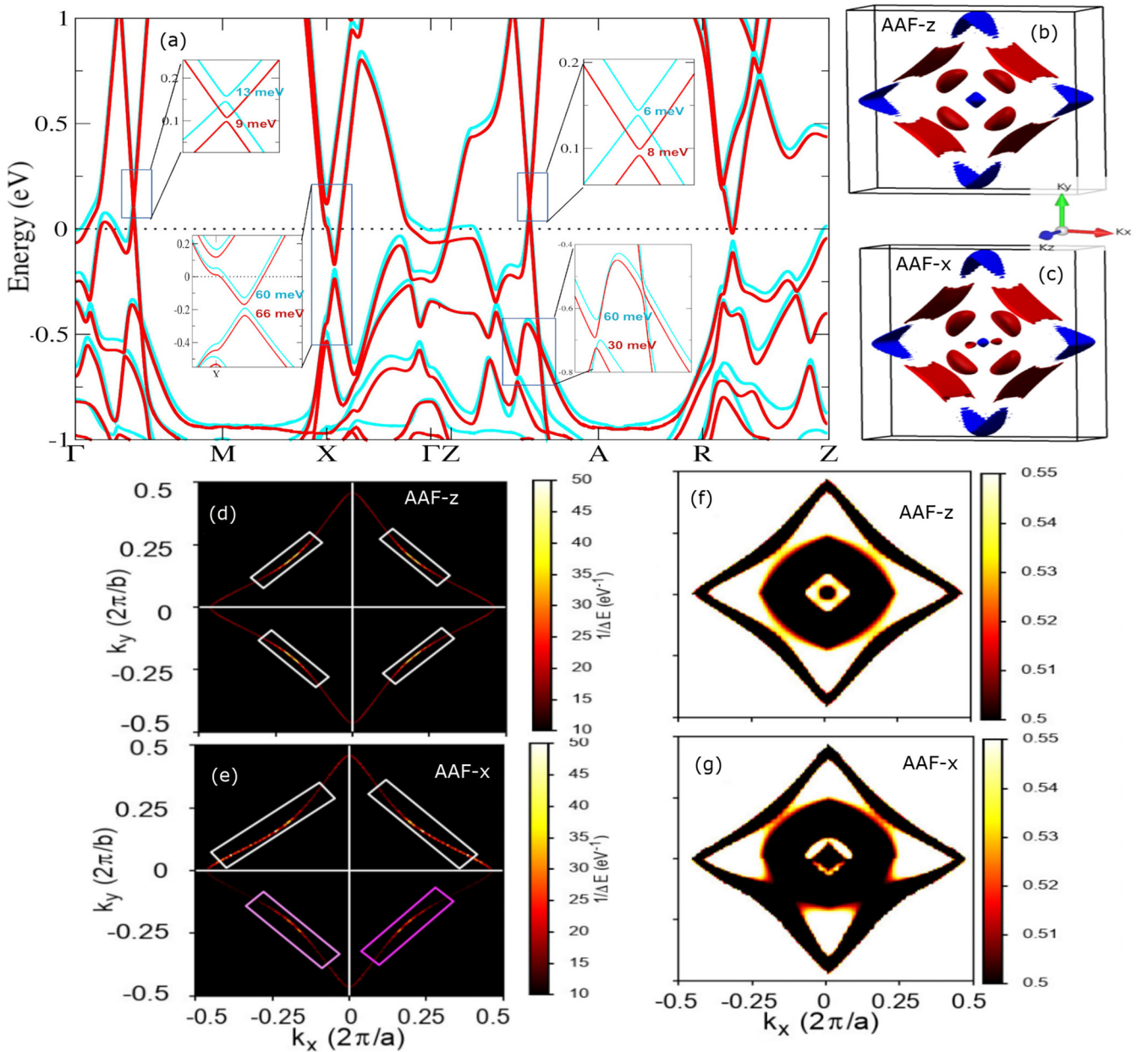
TABLE III. The magnetic symmetry group and symmetry operations of different magnetic patterns. In the first and last two rows, the symmetry operations which are different for the $\hat{x}$ and $\hat{z}$ Néel vector orientations of the same AFM patterns are colored in gray. Other symmetry operations can be generated by the action of $\mathcal{PT}$ for the AAF phase and by the action of $\mathcal{P}$, $\mathcal{T}'$, and $\mathcal{PT}$ for the AAF3 phase, hence not mentioned here for clarity.

Pattern	MSG	Symmetry operations
AAF-z	129.419 ($P4/n'm'm$)	$\{4^+_{001}|\frac{1}{2}00\}$, $\{4^-_{001}|0\frac{1}{2}0\}$, $\{2_{100}|\frac{1}{2}00\}$, $\{2_{010}|0\frac{1}{2}0\}$, $\{2_{001}|\frac{1}{2}\frac{1}{2}0\}$, $\{2_{110}|\frac{1}{2}\frac{1}{2}0\}$, $\{2_{1-10}|0\}$, $\{-1'|0\}$
AAF-x	59.407 ($P_{m'mn}$)	$\{m_{100}|\frac{1}{2}00\}$, $\{2_{010}|0\frac{1}{2}0\}$, $\{m_{001}|\frac{1}{2}\frac{1}{2}0\}$, $\{-1'|0\}$
AAF3-z	130.432 (P_c4/ncc)	$\{4^+_{001}|\frac{1}{2}00\}$, $\{4^-_{001}|0\frac{1}{2}0\}$, $\{2_{110}|\frac{1}{2}\frac{1}{2}\frac{1}{2}\}$, $\{2_{1-10}|00\frac{1}{2}\}$, $\{2_{001}|\frac{1}{2}\frac{1}{2}0\}$, $\{2_{100}|\frac{1}{2}0\frac{1}{2}\}$, $\{2_{010}|0\frac{1}{2}\frac{1}{2}\}$, $\{-1|0\}$, $\{1'|00\frac{1}{2}\}$
AAF3-x	62.450 (P_anma)	$\{2_{001}|\frac{1}{2}\frac{1}{2}\frac{1}{2}\}$, $\{2_{100}|\frac{1}{2}00\}$, $\{2_{010}|0\frac{1}{2}\frac{1}{2}\}$, $\{-1|0\}$, $\{1'|00\frac{1}{2}\}$

FIG. 5. Comparison of the electronic structure between the AAF-$\hat{z}$ and AAF-$\hat{x}$ phases with the inclusion of SOC and U of 6 eV. (a) Band structure along Γ-M-X-Γ-Z-A-R-Z high symmetry direction for the two phases. The cyan (red) lines show bands for magnetization along $\hat{x}$ ($\hat{z}$) direction. (b) and (c) Fermi surface plots on the 3D Brillouin zone with red and blue colors showing hole and electron pockets, respectively. (d) and (e) Intensity plot of the inverse band gap value between the valence and conduction band on the k_x-k_y plane at $k_z = 0$ which shows the formation of the gapped nodal line feature around the Γ point. The rectangular boxes are drawn to highlight the fact that the $\hat{x}$ phase has a broken $\mathcal{R}_4$ symmetry, whereas $\hat{z}$ phase obeys $\mathcal{R}_4$ perfectly. (f) and (g) Contour plot of the Eu-$4f$ orbital distribution on the valence band. The intensity range (color bar) is shown in a narrow region to amplify the small differences between the two magnetic phases. These figures again highlight that $\mathcal{R}_4$ is weakly broken for the $\hat{x}$ phase. See text for details.

the Fermi level and the small DOS at the Fermi level mainly comes from the Sb2 p_x-p_y orbitals.

We find that despite the absence of some symmetries in the AAF-$\hat{x}$ phase, as mentioned in the previous section, the bulk band structure for both phases in the vicinity of the Fermi level looks almost identical except for small momentum dependent shifts. This is expected as the localized Eu-$4f$ orbitals are pushed away from the Fermi level due to the application of the Hubbard U correction. The Fermi surface plots in Figs. 5(b) and 5(c) highlight this fact which show similar features except

for a slight difference at the Γ point. In fact, the electronic dispersion from the nonmagnetic phase (Fig. 2) is not very different from the AAF phase which shows that the effect of magnetism in the electronic dispersion is small in this system. In the absence of SOC, the valence and conduction bands form a gapped nodal line on the k_x-k_y plane with band crossings along the Γ-M direction. All the crossings are gapped by the action of SOC for both phases. This is similar to the case of nodal line semimetal ZrSiS where SOC has been found to open a gap in the Dirac crossings [18].
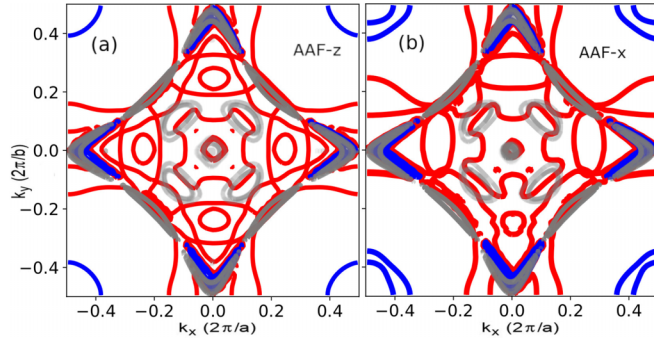
FIG. 6. Comparison of the slab Fermi surface between the (a) AAF-$\hat{z}$ and (b) AAF-$\hat{x}$ phase. The gray lines are the bulk-derived states and the red-blue lines denote the hole and electron Fermi pockets obtained from the three-layer slab calculation. Notice that the broken $\mathcal{R}_4$ symmetry is amplified in the surface dispersion in (b).

Although there are no protected crossings for both phases, the magnitude of the band gap is different for the two magnetic phases. In Figs. 5(d) and 5(e) we show the inverse of the eigenvalue difference between the valence and the conduction bands on the k_x-k_y plane at $k_z = 0$ to highlight the presence of the gapped nodal line feature. In the $\hat{z}$ phase, the gap distribution is identical in all four quadrants, however, that is not the case in the $\hat{x}$ phase. This is a clear signature of the broken global $\mathcal{R}_4$ symmetry on the $\hat{x}$ phase only [Fig. 5(e)]. To understand further the origin of the $\mathcal{R}_4$ symmetry breaking, we also looked at the **k**-dependent valence band occupancy of the $4f$ electrons on the k_x-k_y plane [Figs. 5(f) and 5(g)]. In the vicinity of the Γ point, we find that the $4f$-electron contribution to the valence band is not symmetric across the four quadrants unlike the $\hat{z}$ phase indicating that $\mathcal{R}_4$ symmetry is weakly broken due to the orientation of the Eu-$4f$ magnetic moments.

b. Surface states: We also performed slab calculation to see how the orientation of the Néel vector affects the surface states. Figure 6 shows the slab Fermi surface of the AAF-$\hat{z}$ and $\hat{x}$ phases obtained from a three-layer slab calculation (see Appendix C, Fig. 16, for results from the semi-infinite slab calculation). The surface is terminated on the Zn and Sb1 layers. The slab calculations show a number of additional features compared to the bulk states which are shown as a gray background. The most notable feature which is absent in the bulk dispersion is the closed loop (red lines) state around the Γ point connecting the gray ellipsoids. Remarkably, the surface states are different for the two phases with the breaking of the $\mathcal{R}_4$ symmetry clearly visible now for the $\hat{x}$ phase unlike the subtle differences we found in the bulk-band features. For example, along the Γ-X as well as Γ-M directions, the surface states, especially the hole ones (red lines), are related by the mirror symmetry $\mathcal{M}_x$ but are asymmetric with respect to the $\mathcal{R}_4$ symmetry, i.e., the pockets are not identical along the four quadrants only for the $\hat{x}$ phase. This is amazing given the fact that the slab is not terminated on the Eu atoms and the Eu-$4f$ states have negligible contribution to the Fermi surface. This demonstrates that the magnitude of the broken symmetry in the electronic dispersion are more amplified on the surface compared to the bulk states. Hence, we anticipate

that surface probes could be more suitable for resolving the broken symmetry phases.

In order to understand further how Eu-f states can affect the Fermi surface properties, we have derived an effective Kondo exchange Hamiltonian for the p_x-p_y electrons in the presence of the Eu-f spins in Appendix B. From such effective Hamiltonian analysis, we find that the Eu magnetic moments can affect the dispersion of the itinerant p_x-p_y electrons through exchange coupling which introduces hopping between the p electrons through Eu sites. In addition, we show that depending on the orientation of the Eu-f spins, the band spectrum as well as their spin texture will be different. This will have consequences in the spin transport properties which will be discussed later.

2. AAF3 phase

We also studied another competing AFM phase AAF3 in detail. AAF3 phase requires the doubling of the unit cell along the **c** axis as seen in Figs. 4(c) and 4(d). Unlike the AAF phase, $\mathcal{P}$ is preserved here. Moreover, despite breaking of the $\mathcal{T}$ symmetry, $\mathcal{T}' = \mathcal{T}\tau$, i.e., $\mathcal{T}$ followed by translation $\tau = \{0, 0, \frac{1}{2}\}$ is the symmetry of the system. Such MSG with nonsymmorphic $\mathcal{T}$ falls into type-IV category and has been found in another AFM Dirac material EuCdAs$_2$ [44]. $\mathcal{PT}'$ symmetry makes the bands doubly degenerate throughout the Brillouin zone. In addition, because of the half-translation along with $\mathcal{T}$, there are interesting symmetry properties.

Similar to the AAF magnetic pattern, the $\hat{z}$ phase here has more symmetry compared to the $\hat{x}$ phase due to the direction of the spins. For example, $\mathcal{R}_4^+$ symmetry is preserved for magnetization along $\hat{z}$ direction, whereas it is not preserved for magnetization along $\hat{x}$ or $\hat{y}$ directions. The complete list of symmetry operations are tabulated in Table III.

Following closely the arguments given in Refs. [6,16], we prove that due to the extra rotational symmetries in the AAF3-$\hat{z}$ phase, Dirac band crossings along different high symmetry directions are preserved, whereas they are avoided (or gapped) in the AAF3-$\hat{x}$ phase. First, we find the eigenvalues of the fourfold rotoinversion symmetry operator $\bar{\mathcal{R}}_4^+ = \{\pm - 4_{001}^+ | \frac{1}{2}, 0, 0\}$:

$$(x, y, z) \xrightarrow{\bar{\mathcal{R}}_4^+} \left(y + \tfrac{1}{2}, -x, -z\right) \xrightarrow{\bar{\mathcal{R}}_4^+} \left(-x + \tfrac{1}{2}, -y - \tfrac{1}{2}, z\right)$$
$$\xrightarrow{\bar{\mathcal{R}}_4^+} \left(y, x - \tfrac{1}{2}, -z\right) \xrightarrow{\bar{\mathcal{R}}_4^+} (x, y, z), \quad (2)$$

Hence, $(\bar{\mathcal{R}}_4^+)^4 = -1$ and the eigenvalues are $J_m = e^{i\frac{(2m+1)\pi}{4}}$, where the minus sign is from the spin rotation and $m = 0, 1, 2, 3$ such that

$$J_0 = e^{i\pi/4} = J_3^*, \quad J_1 = e^{i3\pi/4} = J_2^*. \quad (3)$$

Because of the $\mathcal{PT}'$ symmetry, the bands are twofold degenerate throughout the BZ. If $|\psi\rangle$ is the simultaneous eigenstate of the Hamiltonian operator and the $\bar{\mathcal{R}}_4^+$, we would like to find the PT' partner of $|\psi\rangle$. For this we need to find the commutation of $\bar{\mathcal{R}}_4^+$ with $\mathcal{PT}'$:

$$(x, y, z) \xrightarrow{\bar{\mathcal{R}}_4^+} \left(y + \tfrac{1}{2}, -x, -z\right) \xrightarrow{\mathcal{PT}'} \left(-y - \tfrac{1}{2}, x, z - \tfrac{1}{2}\right),$$
$$(x, y, z) \xrightarrow{\mathcal{PT}'} \left(-x, -y, -z - \tfrac{1}{2}\right) \xrightarrow{\bar{\mathcal{R}}_4^+} \left(-y + \tfrac{1}{2}, x, z + \tfrac{1}{2}\right),$$
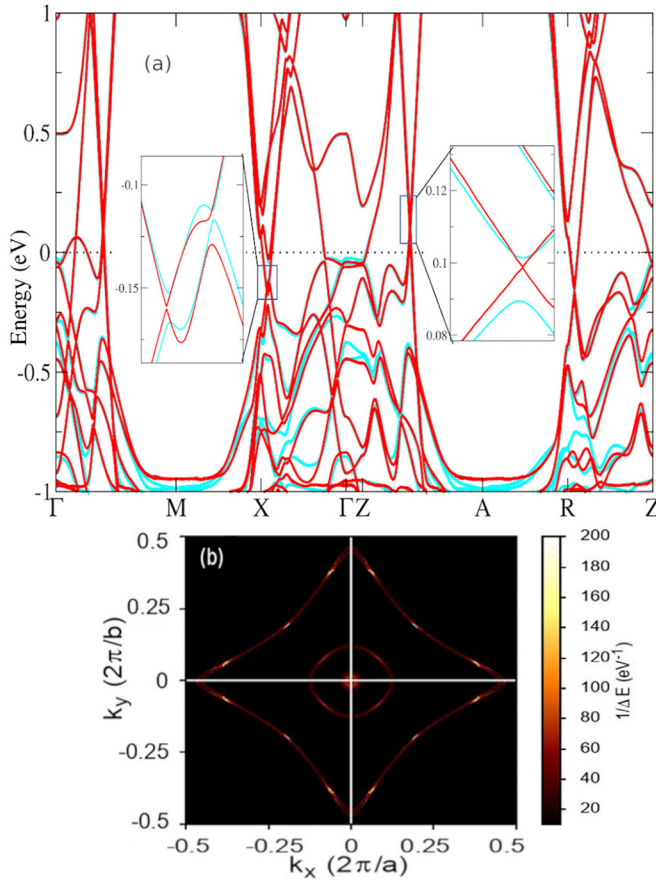$$(4)$$

FIG. 7. (a) Comparison of the electronic dispersion between the AAF3-$\hat{x}$ (cyan) and $\hat{z}$ (red) magnetic phases. The inset shows band crossings near the Fermi level for the $\hat{z}$ phase, whereas the crossing is avoided for the $\hat{x}$ phase. (b) Intensity plot of the inverse band gap between the valence and conduction bands for the $\hat{z}$ phase showing crossings along the Γ-M directions and in the vicinity of the X point. The small gap of ~10 meV seen in the plot is due to the finite **k** mesh.
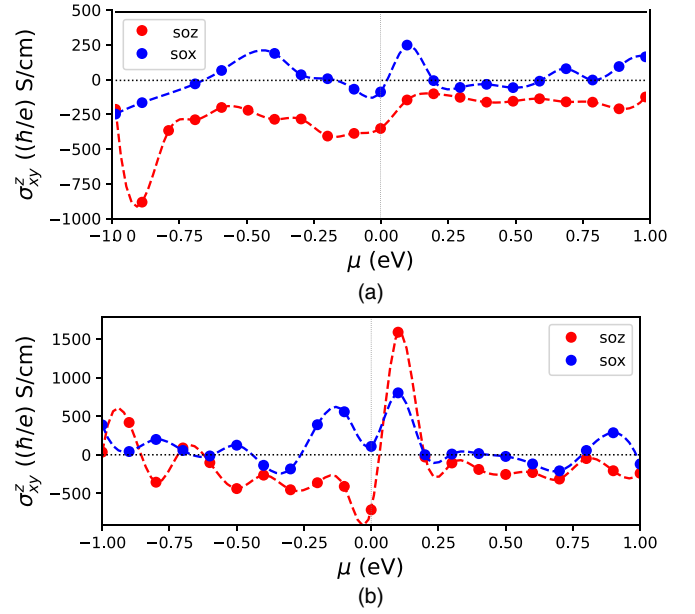

FIG. 8. Comparison of the σ_{xy}^{z} component of the SHC tensor as a function of the chemical potential between the $\hat{x}$ and $\hat{z}$ phases of the (a) AAF and (b) AAF3 magnetic patterns. The dots are calculated values and dashed lines are obtained from cubic spline interpolation.

i.e.,

$$\bar{\mathcal{R}}_4^+ PT' = \tau(1,0,1)\mathcal{P}\mathcal{T}'\bar{\mathcal{R}}_4^+$$

$$\Rightarrow \bar{\mathcal{R}}_4^+ \mathcal{P}\mathcal{T}'|\psi\rangle = e^{-i(k_x+k_z)}PT'\bar{\mathcal{R}}_4^+|\psi\rangle,$$

$$\text{RHS} = e^{-i(k_x+k_z)}\mathcal{P}\mathcal{T}'\bar{\mathcal{R}}_4^+|\psi\rangle$$

$$= e^{-i(k_x+k_z)}\mathcal{P}\mathcal{T}'J_m|\psi\rangle$$

$$= e^{-i(k_x+k_z)}J_m^* e^{(ik_z/2)}\mathcal{P}\mathcal{T}'|\psi\rangle$$

$$= e^{-i(k_x)}e^{-(ik_z/2)}J_m^*\mathcal{P}\mathcal{T}'|\psi\rangle. \quad (5)$$

This implies that if $|\psi\rangle$ is an eigenstate of $\bar{\mathcal{R}}_4^+$ operator with eigenvalue J_m, then $\mathcal{P}\mathcal{T}'|\psi\rangle$ is also an eigenstate of $\bar{\mathcal{R}}_4^+$ with eigenvalue $e^{-i(k_x-k_z/2)}J_m^*$. Now, let us examine the $\bar{\mathcal{R}}_4^+$ eigenvalues of $|\psi\rangle$ and its $\mathcal{P}\mathcal{T}'$ partner at different high symmetry points which are invariant under the $\bar{\mathcal{R}}_4^+$ operation.

At the Γ point, where **k** = **0**, states with $\bar{\mathcal{R}}_4^+$ eigenvalues of (J_0, J_3) and (J_1, J_2) form degenerate pairs. Similarly, at the M high symmetry point $(\pi, \pi, 0)$, because of the extra e^{-ik_x} factor, (J_0, J_2) and (J_1, J_3) form degenerate pairs, i.e., the $\bar{\mathcal{R}}_4^+$ eigenvalues of the Kramer's pairs switches partner

compared to the Γ point. This makes the Dirac band crossing unavoidable along this line. Following similar arguments, we find that there is an unavoidable crossing along the Z-A line.

In Fig. 7(a) we compare the DFT calculated bands between the AAF3-$\hat{x}$ and AAF3-$\hat{z}$ phases. The differences between the two are very small but most importantly there are some crossings in the AAF3-$\hat{z}$ patterns which are absent in the $\hat{x}$ pattern. For example, along the Γ-M and Z-A directions, $\hat{z}$ pattern shows crossings, whereas there is a small gap of ~10 meV in the $\hat{x}$ pattern. A similar feature is seen along the X-Γ and R-Z lines. On the contrary, at the Z point, $\hat{x}$ phase shows fourfold degeneracy, whereas $\hat{z}$ phase has a gap of few meVs. Figure 7(b) shows the plot of inverse of the eigenvalue difference between the valence and conduction band for the AAF3-$\hat{z}$ pattern on the k_x-k_y plane at $k_z = 0$ plane. Similar to the AAF pattern, we see a gapped nodal line feature with a small difference that point nodes survive along Γ-M and Γ-X direction for the AAF3-$\hat{z}$ phase only.

We calculated the topological properties of nonmagnetic and selected magnetic phases of EuZnSb$_2$ using the topological classification scheme of Vergniory $et\ al.$ [45]. We find that the nonmagnetic phase without SOC lies in the enforced semimetal (ES) class which is characterized by the band crossings along different lines at the Fermi level. This is consistent with our band structure results presented in Sec. III B. Such enforced semimetal, in the framework of topological quantum chemistry, can become a topological insulator upon symmetry breakings. In the presence of SOC, all the band crossings are gapped out for the nonmagnetic phase. In this case, the system becomes trivial as the set of bands below the Fermi level can be expressed as a linear combination of elementary band representations (LCEBR). As for the magnetic phases, we performed a similar calculation and found that the AAF-z
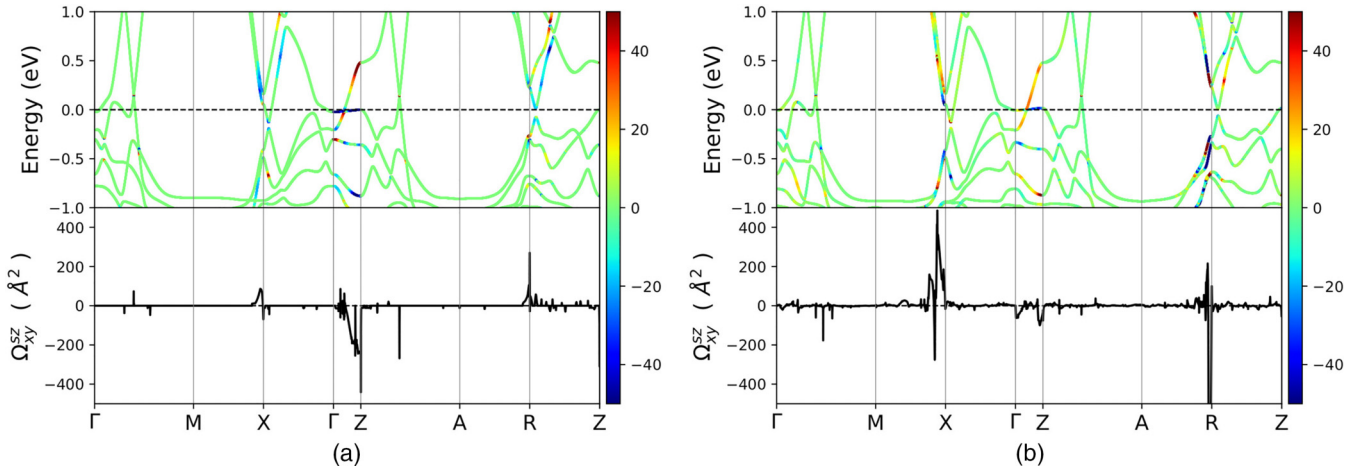
FIG. 9. Comparison of the **k**-resolved spin Berry curvature Ω_{xy}^{sz} between (a) AAF-$\hat{z}$ and (b) AAF-$\hat{x}$ patterns. Top panels: Band structure along high symmetry directions colored by the spin Berry curvature of individual bands $\Omega_{n,xy}^{sz}(\mathbf{k})$. Bottom panels: Sum of the $\Omega_{n,xy}^{z}(\mathbf{k})$ up to the Fermi level along the high symmetry directions.

magnetic phase in the presence of SOC is also topologically trivial (LCEBR) as the band crossings do not survive. On the contrary, for the AAF3-z AFM phase, we find that Dirac band crossings are present in the vicinity of the Fermi level even in the presence of SOC. Such crossings are protected by crystal symmetries, which makes the system topologically nontrivial.

D. Calculation of the spin Hall conductivity and spin current manipulation

In the previous section we saw that the orientation of the Néel vector gives very small changes in the electronic structure. In this section we show that even though the electronic dispersion appears similar, the difference in the spin dependent transport property is appreciable. To highlight this difference, we will study spin Hall conductivity (SHC).

The phenomenon of spin Hall effect corresponds to generation of a purely transverse spin current by the applied electric field [46]. Out of the three mechanisms (intrinsic, skew scattering, and side jump) contributing to the SHC, the intrinsic component of the SHC is a direct consequence of the band topology similar to the phenomenon of anomalous Hall conductivity when the applied electric field generates a transverse charge current. SHC is a third rank tensor and is defined as [41]

$$\sigma_{ab}^{c}(\mu) = -\frac{e^2}{\hbar} \int_{BZ} \frac{d^3\mathbf{k}}{(2\pi)^3} \sum_n f_{n\mathbf{k}}(\mu)\Omega_{n,ab}^{c}(\mathbf{k}), \quad (6)$$

where $f_{n\mathbf{k}}(\mu)$ is the **k**-dependent equilibrium occupation factor of the nth band at the chemical potential of μ. $\Omega_{n,ab}^{c}$ is the band resolved spin Berry curvature which is, in general, a function of **k** and frequency ω and is given by

$$\Omega_{n,ab}^{c}(\omega, \mathbf{k})$$

$$= -2\hbar^2 \sum_{m \neq n} \text{Im} \frac{\langle n\mathbf{k}|\{\hat{\sigma}_c, \hat{v}_a\}|m\mathbf{k}\rangle \langle m\mathbf{k}|\hat{v}_b|n\mathbf{k}\rangle}{\Delta_{nm}^2(k) - (\hbar\omega + i\eta)^2}, \quad (7)$$

where $\hat{v}_i = \frac{\partial}{\partial k_b}$ is the velocity operator, $\hat{\sigma}$ is the Pauli spin matrix, and $\Delta_{nm}(k) = E_{nk} - E_{mk}$. Here we ignore the ω

dependence of the spin Berry curvature. Equation (7) is deceivingly similar to the formula for the normal (charge) Berry curvature; the only difference is that here one has to evaluate the matrix element of the anticommutator between the velocity operator and Pauli matrix instead of just the velocity operator in the normal Berry curvature.

SHC, being a third rank tensor, has 27 components; the magnetic symmetry determines which of them are nonzero. From the symmetry analysis, we find that there are only three (six) independent components for the $\hat{z}(\hat{x})$ phase. The exact form of the SHC tensor for each of these phases is presented explicitly in Table IV. The reason $\hat{x}$ phase has twice the number of independent components compared to the $\hat{z}$ phase is a consequence of the broken tetragonal symmetry due to the broken $\mathcal{R}^4$ symmetry as mentioned before. Note that due to the $\mathcal{PT}$ symmetry, the anomalous Hall conductivity is identically zero in the AFM phase.

In Fig. 8 we compare the σ_{xy}^{z} component for the $\hat{x}$ and $\hat{z}$ Néel vector patterns for both AAF and AAF3 magnetic phases as a function of the chemical potential (μ). Other nonzero components of SHC σ_{yz}^{x} and σ_{zx}^{y} are shown in Appendix B, Fig. 17. σ_{xy}^{z} measures the $\hat{z}$ component of the spin current along the $\hat{x}$ direction in the presence of the external field in the $\hat{y}$ direction. We find that the differences in the SHC value between the $\hat{x}$ and $\hat{z}$ patterns are appreciable. Interestingly, the magnitude of SHC increases by more than twofold for the AAF3 pattern compared to the AAF pattern in the vicinity of the Fermi level. This is likely due to the presence of band crossings or small band gaps in the AAF3 pattern.

Figure 9 shows momentum resolved spin Berry curvature along the high symmetry directions for the $\hat{z}$ and $\hat{x}$ phases of the AAF magnetic pattern. The intensity on the top panels shows the magnitude of the band resolved spin Berry curvature for each **k** value, whereas the bottom panels show the band summation of the **k**-dependent spin Berry curvature up to the occupied states (E_F). These figures highlight the fact that despite the bulk band structure features being similar, the distribution and magnitude of the spin Berry curvature can be different due to the small differences in the band eigenvalues

and spin texture of the bands. Our analysis from the effective Kondo exchange Hamiltonian presented in Appendix B indeed finds that the band dispersion and their spin texture will be different depending on the orientation of the Néel vector.

Recent experiments [13,14] demonstrate that the direction of the Néel vector can be manipulated by external means like spin-current injection. Quantifying the changes in the spin Hall conductivity and electronic dispersion experimentally by varying the magnetization direction is important to determine the validity of our calculation methods. In addition, many novel phenomena for spin-current generation and control has been recently predicted in a wide variety of AFM materials [47–49]. It will be interesting to explore such effects in future theoretical as well as experimental studies in related systems.

IV. CONCLUSIONS AND OUTLOOK

In summary, we have studied the electronic structure and magnetic properties of an antiferromagnetic square-net topological semimetal $EuZnSb_2$ by employing the first-principles and effective Hamiltonian methods. We have found that the effect of magnetism on the bulk low energy spectrum, especially that introduced by the orientation of the Néel vector, is weak. Despite such weak effects in the bulk dispersion, we find that there are consequences for the transport properties and surface electronic dispersion. For example, our calculations predict that the broken symmetry introduced by the direction of the Néel vector is amplified in the surface electronic dispersion. Similarly, the differences in the spin Hall conductivity response between different magnetic phases is appreciable. We derived an effective Kondo exchange Hamiltonian to understand our main findings. It will be interesting to confirm some of the predictions made in this study by experiments like ARPES in conjunction with the spin-orbit torque experiments that can control the orientation of the Néel vector [15]. Because of the presence of the competing magnetic states which depend on the strength of the interaction term in our calculations, it will also be intriguing to study the possibilities of controlling the magnetic ground state and the band topology by means of small external perturbations like pressure, doping, intercalation, chemical substitution, etc. Similarly, study of the surface magnetism, surface transport properties, etc. could be other directions in these investigations.

To conclude, our work provides compelling evidence that study of the f-electron AFM can be a promising field for band engineering and spintronics applications. Similar investigations are necessary for other predicted f-electron square-net systems in order to make systematic comparisons and predictions. We believe that our study will motivate future works in this direction, especially towards prediction and search of Dirac materials showing large electronic response to the magnetic texture, using more sophisticated numerical techniques.

ACKNOWLEDGMENT

TABLE IV. The form of the spin Hall conductivity tensor for the $\hat{x}$ and $\hat{z}$ magnetic phases for both AAF and AAF3 magnetic patterns.

	σ^x			σ^y			σ^z		
$\hat{z}$ phase	$\begin{pmatrix} 0 & 0 & 0 \\ 0 & 0 & -\sigma^y_{xz} \\ 0 & -\sigma^y_{zx} & 0 \end{pmatrix}$			$\begin{pmatrix} 0 & 0 & \sigma^y_{xz} \\ 0 & 0 & 0 \\ \sigma^y_{zx} & 0 & 0 \end{pmatrix}$			$\begin{pmatrix} 0 & -\sigma^z_{yx} & 0 \\ \sigma^z_{yx} & 0 & 0 \\ 0 & 0 & 0 \end{pmatrix}$		
$\hat{x}$ phase	$\begin{pmatrix} 0 & 0 & 0 \\ 0 & 0 & \sigma^x_{yz} \\ 0 & \sigma^x_{zy} & 0 \end{pmatrix}$			$\begin{pmatrix} 0 & 0 & \sigma^y_{xz} \\ 0 & 0 & 0 \\ \sigma^y_{zx} & 0 & 0 \end{pmatrix}$			$\begin{pmatrix} 0 & \sigma^z_{xy} & 0 \\ \sigma^z_{yx} & 0 & 0 \\ 0 & 0 & 0 \end{pmatrix}$		

APPENDIX A: NONMAGNETIC PHASE AND WANNIER TIGHT BINDING

1. Band characters

In Fig. 10 we show the orbital composition of the bands (or band characters) in the vicinity of the Fermi level for the nonmagnetic phase.
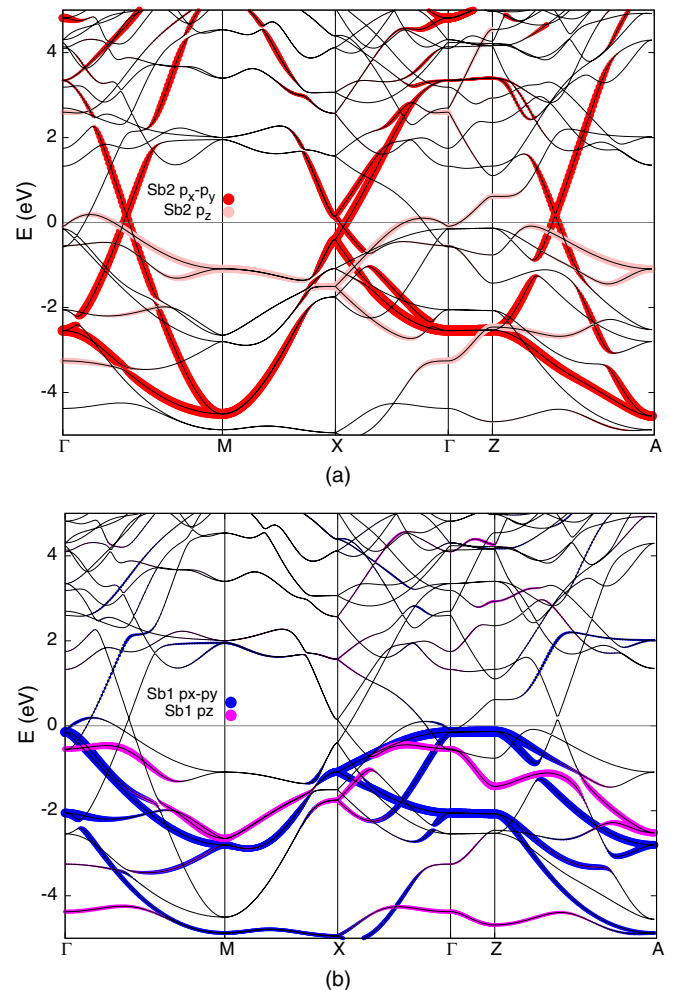

FIG. 10. Character of the bands in the vicinity of the Fermi level for nonmagnetic phase in the absence of SOC: (a) Sb2 p_x-p_y and p_z character and (b) Sb1 p_x-p_y and p_z character .The size of the dots is proportional to the orbital composition of the particular state.
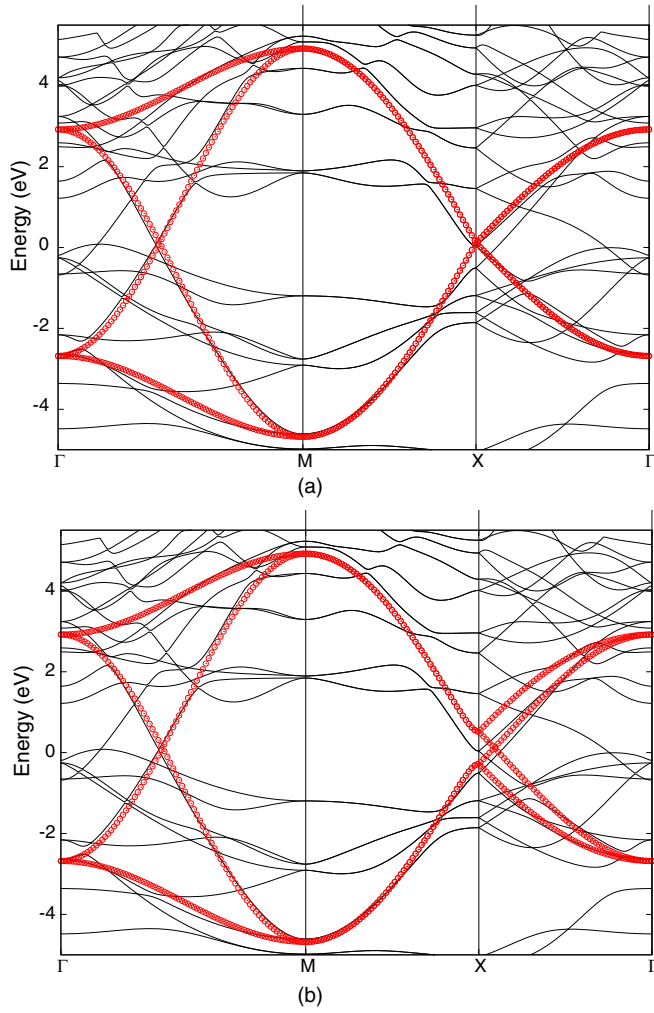
FIG. 11. Wannier bands (red dots) from a 4×4 Hamiltonian formed by the p_x-p_y orbitals of the Sb2 square lattice by considering up to the (a) nn and (b) nnn hopping terms given in Table I.

2. Wannier bands

In Figs. 11 and 12 we compare the eigenvalues obtained from different tight-binding Wannier Hamiltonian forms with DFT calculated bands for the nonmagnetic phase.

3. Analytical expression of the eigenvalues for the 4×4 TB Hamiltonian

In this subsection we derive the 4×4 TB Hamiltonian for noninteracting band electrons whose parameters are given in the main text. For concreteness we define a $\sqrt{2} \times \sqrt{2}$ square lattice containing two atoms in the unit cell with lattice vectors $\vec{a} = a_0(\hat{x}, -\hat{y})$, $\vec{b} = a_0(\hat{x}, \hat{y})$, where a_0 is the distance between the nearest neighbor atoms of the primitive square lattice unit cell. The tight-binding Hamiltonian in $\mathbf{k}$ space for such two-atom and two-orbital systems without spin-orbit coupling is

$$\hat{H}_0 = \sum_{\mathbf{k}} c_{\mathbf{k}}^{\dagger} H_0(\mathbf{k}) c_{\mathbf{k}}, \tag{A1}$$

where $c_{\mathbf{k}}^{\dagger} = (c_{\mathbf{k}_{p_x}}^{1\dagger}, c_{\mathbf{k}_{p_y}}^{1\dagger}, c_{\mathbf{k}_{p_x}}^{2\dagger}, c_{\mathbf{k}_{p_y}}^{2\dagger})$ such that $c_{\mathbf{k}_{p_x}}^{1\dagger}$ creates an electron at the p_x Wannier orbital located at site 1 and so on.
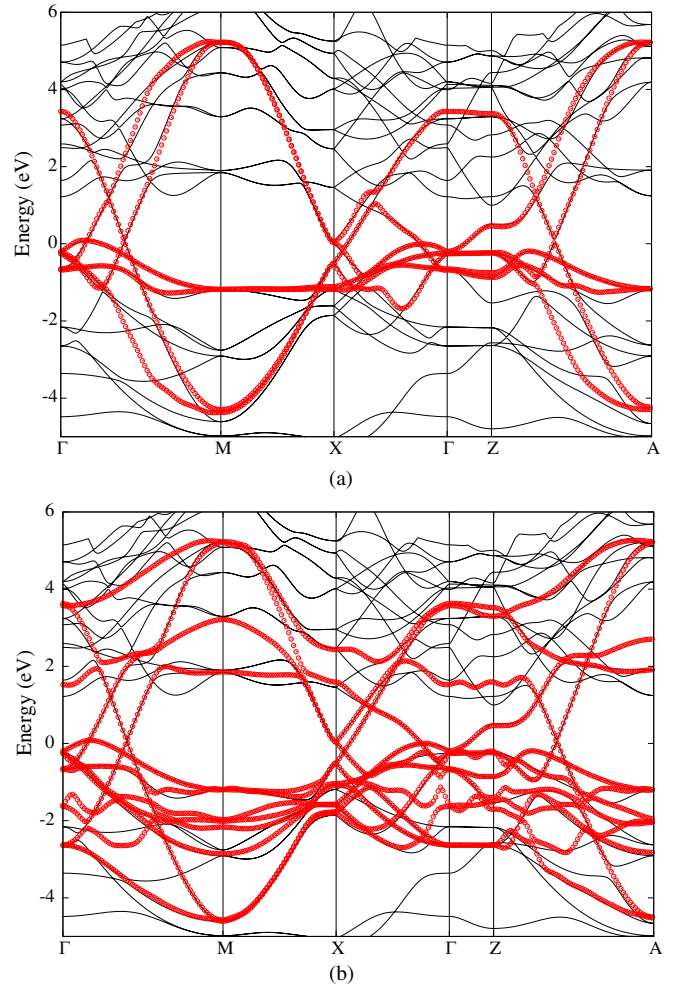

FIG. 12. (a) 6×6 and (b) 12×12 Wannier bands (red dots) superimposed onto the DFT bands (black lines). Long range hooping terms are included in the Wannier Hamiltonian to reproduce the bands exactly.

Similarly, the Hamiltonian matrix in this basis is given by

$$H_0(\mathbf{k}) = \begin{pmatrix} t_{\mathbf{k}}'' & t_{\mathbf{k}}' & t_{\mathbf{k}_{\sigma\pi}} & 0 \\ t_{\mathbf{k}}' & t_{\mathbf{k}}'' & 0 & t_{\mathbf{k}_{\pi\sigma}} \\ t_{\mathbf{k}_{\sigma\pi}} & 0 & t_{\mathbf{k}}'' & t_{\mathbf{k}}' \\ 0 & t_{\mathbf{k}_{\pi\sigma}} & t_{\mathbf{k}}' & t_{\mathbf{k}}'' \end{pmatrix}, \tag{A2}$$

where we have defined the hopping matrix elements as follows: $t_{\mathbf{k}_{\sigma\pi}} = -2[t_{\sigma} \cos(k_x a_0) + t_{\pi} \cos(k_y a_0)]$, $t_{\mathbf{k}_{\pi\sigma}} = -2[t_{\pi} \cos(k_x a_0) + t_{\sigma} \cos(k_y a_0)]$ and $t_{\mathbf{k}}' = 4t' \sin(k_x a_0) \sin(k_y a_0)$, $t_{\mathbf{k}}'' = 2t''[\cos(2k_x a_0) + \cos(2k_y a_0)]$ and $t_{\sigma} = -1.9$ eV, $t_{\pi} = 0.5$ eV, $t' = 0.1$ eV, and $t'' \sim 0.04$ eV. t_{σ} and t_{π} are the nearest neighbor σ and π hoppings, respectively, and t', t'' are the next-nearest and the third neighbor hopping matrix elements. Note that the $t_{\mathbf{k}}''$ term, which introduces $\mathbf{k}$-dependent shift of the bands, is included here for better comparison with the DFT results and does not change the main conclusions. The eigenvalues of $H(\mathbf{k})$ are

$$E_0(\mathbf{k}) = t_{\mathbf{k}}'' \pm \frac{1}{2}\left\{ t_{\mathbf{k}_{\sigma\pi}} + t_{\mathbf{k}_{\pi\sigma}} \pm \left[(t_{\mathbf{k}_{\sigma\pi}} - t_{\mathbf{k}_{\pi\sigma}})^2 + 4(t_{\mathbf{k}}')^2 \right]^{1/2} \right\}. \tag{A3}$$
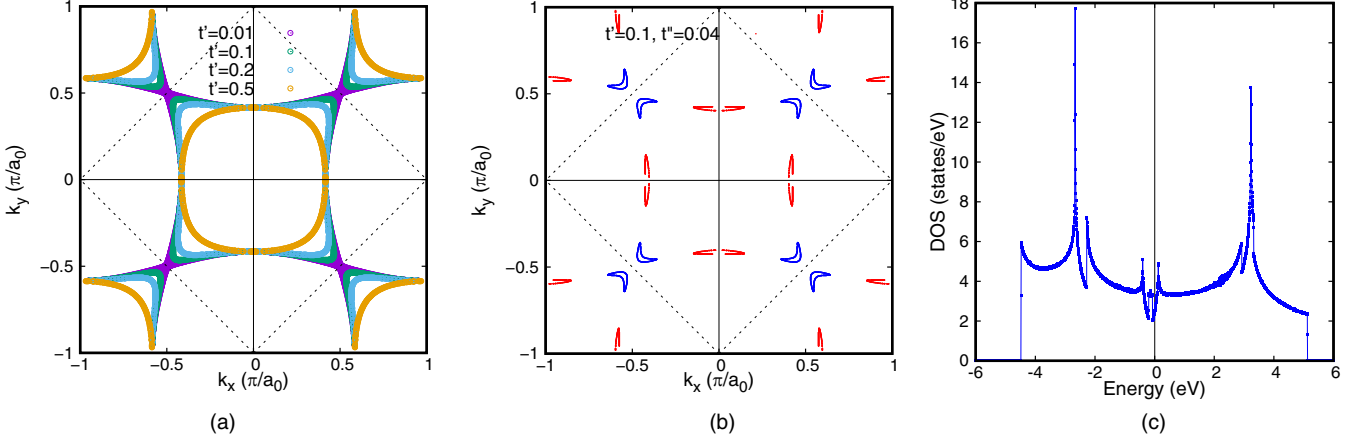
FIG. 13. (a) Fermi surface (FS) of the 4×4 tight-binding Hamiltonian in the extended zone scheme for different values of t' with $t'' = 0$ at half-filling and without SOC. SOC opens the gap in the spectrum for $t'' = 0$ case. (b) and (c) FS and density of states, respectively, with SOC for $t'' = 0.04$ eV. The chemical potential is tuned to make the system compensated which corresponds to $E \sim 0.014$ eV in (c). The red and blue colored FS pieces denote hole and electron pockets in (b). The dashed lines in (a) and (b) show the reduced Brillouin zone.

First we discuss the condition when $t'' = 0$ where particle-hole symmetry is preserved. The situation of half-filling corresponds to zero chemical potential. Then the Fermi surface is determined by the zero energy solution of Eq. (A3):

$$(t_{\mathbf{k}_{\sigma\pi}} t_{\mathbf{k}_{\pi\sigma}} - t_{\mathbf{k}}'^2) = 0. \tag{A4}$$

This condition gives a diamond-shaped Fermi surface as shown in Fig. 13(a). When the nnn hopping strength is increased, the Fermi surface becomes more circular and shifts away from the zone boundary (X point).

For $t' = 0$, the eigenvalues have a trivial form given by

$$E_0(\mathbf{k}) = \pm t_{\mathbf{k}_{\sigma\pi}} \text{ and } t_{\mathbf{k}_{\pi\sigma}}. \tag{A5}$$

When $|k_x| = |k_y| = k_0$, the eigenvalues are $\pm 2(t_\sigma + t_\pi)\cos(k_0 a_0)$. This gives degenerate bands along this line as seen along the Γ-X and M-X line in Fig. 11(a).

We see that in the absence of further interactions we have a metal with a half-filled conduction band. Such a situation is unstable with respect to unit cell doubling which can gap out (at least partially) the Fermi surface. Such unit cell doubling can occur already on the single particle level or be a

consequence of the interactions. Below we consider the former mechanism first.

The spin-orbit coupling (SOC) is of the form

$$H_{\mathrm{SOC}} = \sigma^z(\lambda \tau_y \otimes I + \delta \tau_z \otimes \gamma_z), \tag{A6}$$

where λ and δ are constants and γ, σ, τ are the Pauli matrices acting on the site, spin, and orbital indices, respectively. Such form of SOC does not couple the $|\uparrow\rangle$ and $|\downarrow\rangle$ spin sectors; hence we can still diagonalize the Hamiltonian analytically. The eigenvalue for each spin sector in the presence of SOC is given by

$$E_{\mathrm{SOC}}(\mathbf{k}) = \pm\sqrt{X(\mathbf{k})^2 + \delta^2} + t''(\mathbf{k}),$$
$$X^2(\mathbf{k}) = \tfrac{1}{4}\{t_{\mathbf{k}_{\sigma\pi}} + t_{\mathbf{k}_{\pi\sigma}} \pm [(t_{\mathbf{k}_{\sigma\pi}} - t_{\mathbf{k}_{\pi\sigma}})^2 + 4(\lambda^2 + t_{\mathbf{k}}'^2)]^{1/2}\}^2. \tag{A7}$$

The estimate is $\delta \approx 0.1$ eV. For $t'' = 0$, the FS is fully gapped at half-filling as discussed in the main text. However, for the $t'' \neq 0$ case, the FS is partially gapped. In Fig. 13(b) we show the FS in the presence of SOC for nonzero t'' at the value of chemical potential when the system is fully compensated. As seen in the figure, there are electron and hole pockets at

TABLE V. Hybridization matrix element (in eV) between the occupied $|\mathrm{Eu}f\sigma\rangle$ and the $|p\sigma\rangle$ states from the Sb2 square nets in the antiferromagnetic configuration without SOC obtained from the Wannier function analysis. For Eu1 atoms, the $|\uparrow\rangle$ states are occupied, whereas for Eu2 atoms, $|\downarrow\rangle$ states are occupied. The matrix elements between the $|p^2\sigma\rangle$ and $|\mathrm{Eu}\sigma\rangle$ states are similar with $p_x \leftrightarrow p_y$. The sign of the matrix elements are fixed by the symmetry of the corresponding hopping integral. Note that the p orbitals in this table are aligned along Eu atoms and vice versa.

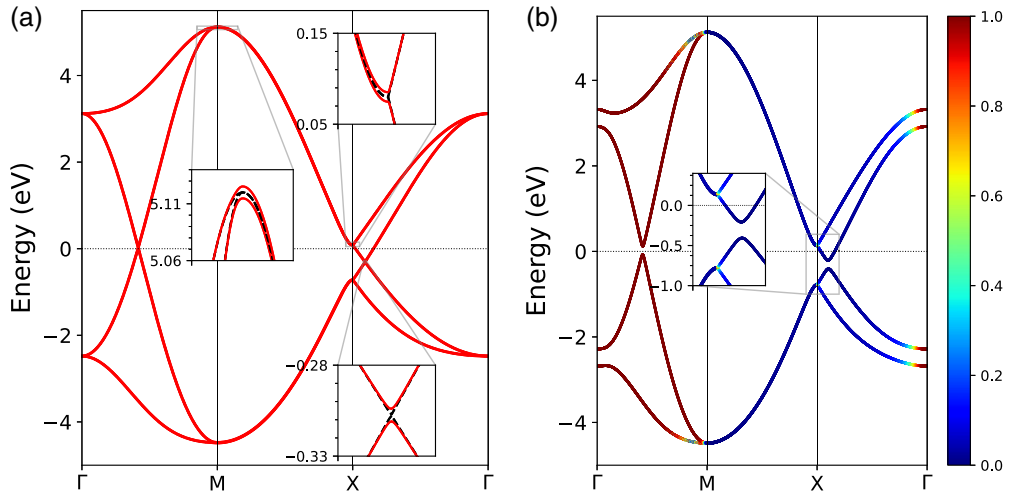| $\langle WFs|H|WFs\rangle$	Eu1-$f_{xz^2}\uparrow$	Eu1-$f_{yz^2}\uparrow$	Eu1-$f_{z^3}\uparrow$	Eu1-$f_{x(x^2-3y^2)}\uparrow$	Eu1-$f_{y(3x^2-y^2)}\uparrow$	Eu1-$f_{z(x^2-y^2)}\uparrow$	Eu1-$f_{xyz}\uparrow$
$p_x^1\uparrow$	-0.13	0	-0.05	-0.03	0	-0.11	0.0
$p_y^1\uparrow$	0	0.01	0	0	0.07	0	0.07
$p_z^1\uparrow$	-0.11	0	0.06	-0.06	0	-0.13	0
$\langle WFs|H|WFs\rangle$	Eu2-$f_{xz^2}\downarrow$	Eu2-$f_{yz^2}\downarrow$	Eu2-$f_{z^3}\downarrow$	Eu2-$f_{x(x^2-3y^2)}\downarrow$	Eu2-$f_{y(3x^2-y^2)}\downarrow$	Eu2-$f_{z(x^2-y^2)}\downarrow$	Eu2-$f_{xyz}\downarrow$
$p_x^1\downarrow$	0.01	0	0	-0.07	0	0	0.07
$p_y^1\downarrow$	0	-0.13	-0.05	0	0.03	0.11	0
$p_z^1\downarrow$	0	-0.11	0.06	0	0.06	0.13	0

FIG. 14. A band structure of the nnn 4×4 tight-binding Hamiltonian in the presence of the effective Kondo exchange Hamiltonian for the AFM arrangement of the Eu-f spins. (a) A comparison with the eigenvalues without the exchange Hamiltonian (black dots) at zero spin-orbit coupling (SOC). Notice that the Kondo exchange splits the band degeneracies by $\sim J_K \langle S \rangle$ at the M, X, and along X-Γ direction. The crossing along Γ-M is preserved by Kondo exchange in the absence of SOC. The dispersion is identical for any orientation of the Néel magnetization. (b) Band dispersion in the presence of Kondo exchange with SOC when the spin quantization axis is along the $\hat{x}$ direction. The color palette shows the magnitude of the $\langle \hat{\sigma}_z \rangle$.

the X point and along Γ-M direction, respectively, similar to the FS of the real system with small DOS at the Fermi level [Fig. 13(c)].

APPENDIX B: DERIVATION OF THE EXCHANGE HAMILTONIAN

In order to understand how the Eu-$4f$ states may affect the band structure and the Fermi surface properties, we have also
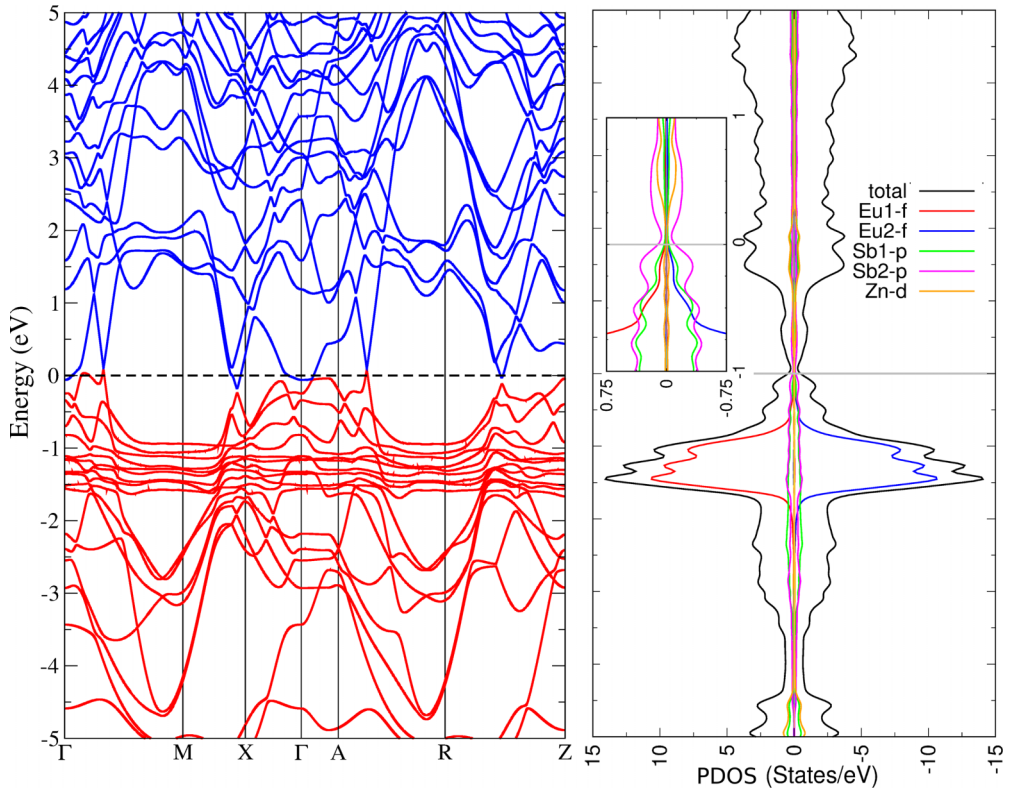

FIG. 15. DFT bands and projected density of states (PDOS) for AAF-$\hat{z}$ magnetic pattern. Positive (negative) PDOS values indicate up (down) states. The minority spin states for AFM aligned Eu-$4f$ electrons are ~ 10 eV above E_F, hence not shown here. The small DOS at E_F comes from Sb2 p_x-p_y orbitals.
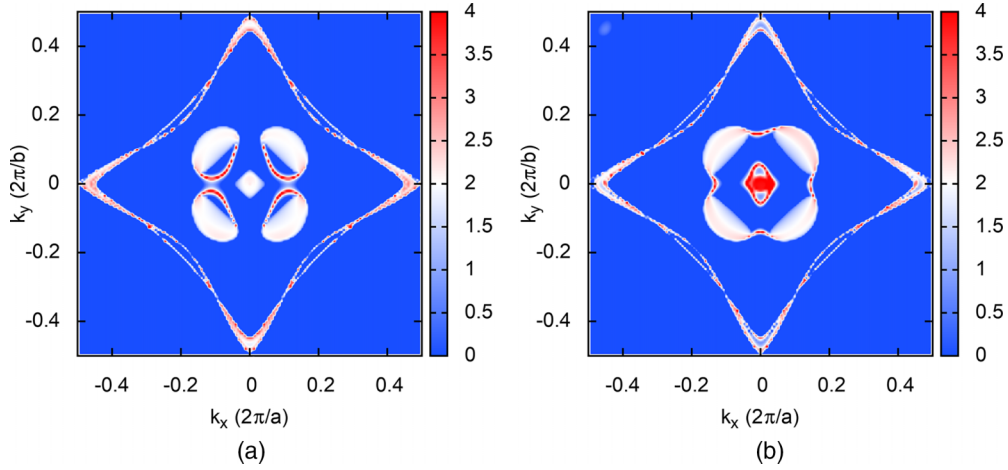
FIG. 16. Slab Fermi surface from semi-infinite layer derived from Wannier Hamiltonian for (a) AAF-$\hat{z}$ and (b) AAF-$\hat{x}$ magnetic patterns. The intensity shows the contribution of the surface states. The system is terminated on the Zn layer.

derived an effective Kondo exchange Hamiltonian within the second order perturbation theory in V. The $4f$ shell of Eu ions is half-filled. The Hund's rule dictates that at the ground state the Eu ion has zero angular momentum and the total spin is $S = 7/2$. Then, according to Ref. [50], the effective Kondo Hamiltonian for an Eu ion located at the origin is the multichannel Kondo model. For a spherically symmetric case it would have the following form:

$$H_{\alpha\beta}^{\text{ex}} = J_K \sum_m c_{m\alpha}^\dagger(|k|)(\vec{\sigma}\vec{S})_{\alpha\beta} c_{m\beta}(|k|), \qquad \text{(B1)}$$

where m are the electron orbital quantum numbers and α, β are spin indices. In the limit when the Hund's coupling exceeds the Kondo temperature [50], the Kondo coupling is given by

$$J_K = \frac{V^2}{2S}[-1/\epsilon_f + 1/(\epsilon_f + U)], \qquad \text{(B2)}$$

with V being the overall scale of the hybridization strength between the Eu-f and conduction electrons (p electrons here) and ϵ_f being the energy levels of the f states. We estimate $J_K \sim 16$ K.

The exchange Hamiltonian is derived under the assumption that the hybridization matrix elements are equal for all orbitals involved in the screening of the spin. For the model on a lattice the latter assumption no longer holds. One has to recalculate the spherical orbitals into the Wannier functions basis as the mth orbital will have its own exchange $\sim |V_m|^2$ which will lead to exchange anisotropy.

By using the hybridization matrix elements between the localized Eu-$4f$ and the itinerant p_x-p_y orbitals from the *ab initio* calculations as shown in Table V, we obtain the following effective Kondo exchange Hamiltonian in the basis of the p orbitals $c_{\mathbf{k}\sigma}^\dagger = (c_{\mathbf{k}_{px}\sigma}^{1\dagger}, c_{\mathbf{k}_{py}\sigma}^{1\dagger}, c_{\mathbf{k}_{px}\sigma}^{2\dagger}, c_{\mathbf{k}_{py}\sigma}^{2\dagger})$:

$$H_{\sigma\sigma'}^{\text{ex}} = J_K \sum_{k,k',R_1} c_{\mathbf{k}\sigma}^\dagger \hat{g}_+(\mathbf{k}, \mathbf{k}')(\vec{\sigma}\vec{S}_{\mathbf{R}_1})_{\sigma,\sigma'} e^{-i(\mathbf{k}-\mathbf{k}')\mathbf{R}_1} c_{\mathbf{k}'\sigma'}$$
$$+ J_K \sum_{k,k',R_2} c_{\mathbf{k}\sigma}^+ \hat{g}_-(\mathbf{k}, \mathbf{k}')(\vec{\sigma}\vec{S}_{\mathbf{R}_2})_{\sigma\sigma'} e^{-i(\mathbf{k}-\mathbf{k}')\mathbf{R}_2} c_{\mathbf{k}'\sigma'},$$

where $\vec{S}_{\mathbf{R}_1}$ and $\vec{S}_{\mathbf{R}_2}$ are the spins localized on the $\mathbf{R}_1$ and $\mathbf{R}_2$ sites. g_+ and g_- are the effective exchange matrices given by

$$g_+(\mathbf{k}, \mathbf{k}') = \begin{pmatrix} g_1 & -g_2 & g_3 - g_4 & -g_3 - g_4 \\ -g_2 & g_1 & g_3 + g_4 & -g_3 + g_4 \\ \text{H.c.} & \text{H.c.} & g_1 & g_2 \\ \text{H.c.} & \text{H.c.} & g_2 & g_1 \end{pmatrix},$$

$$g_-(\mathbf{k}, \mathbf{k}') = \begin{pmatrix} g_1 & g_2 & g_3 - g_4^* & g_3 + g_4^* \\ g_2 & g_1 & -g_3 - g_4^* & -g_3 + g_4^* \\ \text{H.c.} & \text{H.c.} & g_1 & -g_2 \\ \text{H.c.} & \text{H.c.} & -g_2 & g_1 \end{pmatrix},$$
$$\text{(B3)}$$

and $\quad g_1 = 1, \quad g_2 = 1/2, \quad g_3 = As_x^*(\mathbf{k})s_y^*(\mathbf{k}'), \quad g_4 = Bs_x^*(\mathbf{k})s_y(\mathbf{k}'), s_a = 1 - e^{-ik_a}, A = 1/16, B = 3/16$.

The role of the Eu magnetic moments: The interaction between conduction electrons and magnetic moments may lead to many different effects. Depending on how strong the coupling is between these two subsystems, the net result many be very different. Below we will consider two scenarios.

In both cases we will treat the Eu spins in the mean-field approximation, that is as classical vectors $\vec{S} = \pm\langle S \rangle \vec{n}$, where $\vec{n}$ is a unit vector and $\langle S \rangle < 7/2$ is the average magnetization which has to be determined self-consistently.

First, we consider the case with zero SOC. Then we will discuss the case with strong SOC δ (we will formulate the precise criterion later). In the latter case, the band electrons are partially gapped with small density of states at the Fermi level and the influence of the spin order on their spectrum is small. The nature of the spin order is determined by the interaction between the spins through the conduction electrons.

Consider spins with opposite directions on $\mathbf{R}_1$ and $\mathbf{R}_2$ sites. Then the Kondo exchange (B3) becomes an effective modification of the spin-orbit coupling:

$$H_{\text{MF}}^{\text{ex}} = 2J_K\langle S \rangle \sum_k c_{\mathbf{k}}^\dagger(\vec{\sigma}\vec{n})[g_2\tau^x \otimes \gamma^z + \text{Im}\,mg_4\tau^z \otimes \gamma^y$$
$$+ \text{Im}\,mg_3\tau^y \otimes \gamma_x - (\text{Re}\,eg_3 + \text{Re}\,eg_4)\tau^y \otimes \gamma^y]c_{\mathbf{k}}.$$
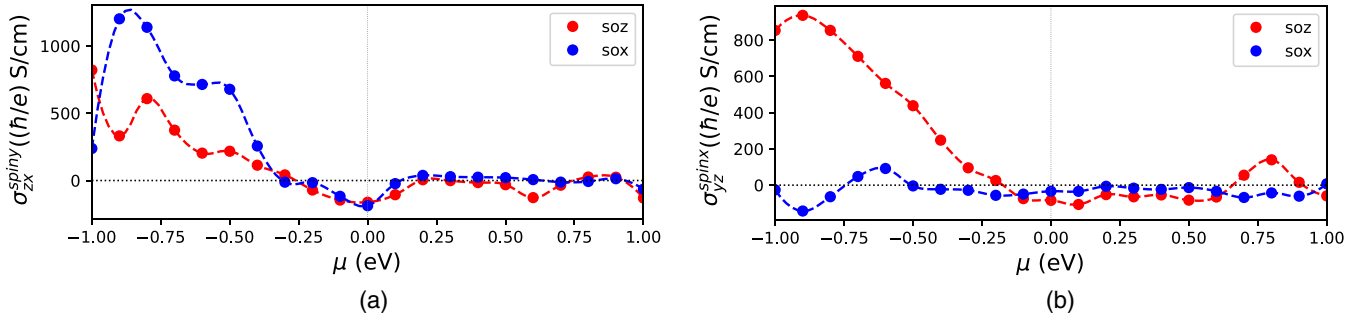$$\text{(B4)}$$

FIG. 17. Comparison of the (a) σ_{yz}^x and (b) σ_{zx}^y component of the SHC tensor as a function of the chemical potential between the AAF-$\hat{x}$ and $\hat{z}$ patterns.

In Fig. 14(a) we show the band dispersion of the p electrons in the presence of the Kondo exchange term for zero SOC. The antiferromagnetic order splits the band dispersion at several places by magnitude of $\sim J_K \langle S \rangle$ which are highlighted in the figure insets.

In order to study the differences in the spectrum due to the spin orientation of the Néel vector, we will need to combine (A6) and (B4). Close to the X point $(\pi/2, \pi/2)$, $t_{\sigma\pi} \sim t_{\pi\sigma} \sim 0$, i.e., there is no coupling between the two sublattices and one can derive the effective Hamiltonian for just one of the sublattice:

$$H_1 = H_2 = \mathcal{O}(J_K^2 \langle S \rangle^2) + t_\mathbf{k}''$$
$$\times \tau^x (t_\mathbf{k}' - 2J_K \langle S \rangle g_2 \sigma^z) + (\vec{\sigma}\vec{n})(\delta\tau^z + \lambda\tau^y). \quad (B5)$$

If the Néel magnetization is along the z axis, the spectrum is

$$E = \mathcal{O}(J_K^2 \langle S \rangle^2) + t_\mathbf{k}''$$
$$\pm [\delta^2 + \lambda^2 + (t_\mathbf{k}' - 2J_K \langle S \rangle g_2 \sigma^z)^2]^{1/2}. \quad (B6)$$

If it is perpendicular to z axis, then

$$E = \mathcal{O}(J_K^2 \langle S \rangle^2) + t_\mathbf{k}''$$
$$\pm \left(\sqrt{t_\mathbf{k}'^2 + \lambda^2 + \delta^2} \pm 2J_K \langle S \rangle g_2 \right). \quad (B7)$$

With our estimates of J_K and δ, we conclude that the first term can be neglected. Thus, we find that there is a small effect in the spectrum due to the rotation of the Eu spins which nevertheless remain partially gapped due to the SOC. More importantly, if $\vec{n}$ is directed along the $\hat{z}$ axis, the z projection of electron spin is a good quantum number. For all other directions it is not. This can be seen from the spin texture of the bands for the $\hat{x}$ phase along the high symmetry directions

in Fig. 14(b). Such differences in the spin texture between the $\hat{z}$ and $\hat{x}$ phases can introduce differences in the spin transport properties like spin Hall conductivity which is proportional to the matrix element of the spin operator.

APPENDIX C: ELECTRONIC DISPERSION AND SPIN HALL CONDUCTIVITY RESULTS FOR MAGNETIC PHASES FROM DFT CALCULATIONS

1. Bulk bands and DOS

Figure 15 shows the DFT calculated bulk electronic bands and DOS for AAF-$\hat{z}$ magnetic phase in the presence of SOC and U of 6 eV.

2. Slab dispersion

In the main text we showed the differences in Fermi surface dispersion between the AAF-$\hat{x}$ and AAF-$\hat{z}$ phases from a 3L slab calculation. In order to confirm that the differences are real, we have also calculated the surface Fermi dispersion from a semi-infinite layer model derived from the Wannier Hamiltonian using the Green's function method as implemented in the WANNIERTools software [51] (Fig. 16). Similar to our conclusions in the main text, we find that despite the bulk states being similar, the surface states and their connectivities are different for different directions of the Néel vector.

3. Comparison with other components of the spin Hall conductivity

In the main text we showed the comparison between the spin Hall conductivity (SHC) response as a function of the chemical potential between the $\hat{x}$ and $\hat{z}$ phase for just one component of the SHC tensor. Here we also show the comparison with other components of the SHC tensor.

[1] Q. Wang, Y. Xu, R. Lou, Z. Liu, M. Li, Y. Huang, D. Shen, H. Weng, S. Wang, and H. Lei, Nat. Commun. **9**, 3681 (2018).

[2] R. Li, J. Wang, X.-L. Qi, and S.-C. Zhang, Nat. Phys. **6**, 284 (2010).

[3] L. Šmejkal, Y. Mokrousov, B. Yan, and A. H. MacDonald, Nat. Phys. **14**, 242 (2018).

[4] M. M. Otrokov, I. I. Klimovskikh, H. Bentmann, D. Estyunin, A. Zeugner, Z. S. Aliev, S. Gaß, A. U. B. Wolter, A. V. Koroleva, A. M. Shikin, M. Blanco-Rey, M.

Hoffmann, I. P. Rusinov, A. Y. Vyazovskaya, S. V. Eremeev, Y. M. Koroteev, V. M. Kuznetsov, F. Freyse, J. Sánchez-Barriga, I. R. Amiraslanov et al., Nature (London) **576**, 416 (2019).

[5] F. Máca, J. Mašek, O. Stelmakhovych, X. Martí, H. Reichlová, K. Uhlířová, P. Beran, P. Wadley, V. Novák, and T. Jungwirth, J. Magn. Magn. Mater. **324**, 1606 (2012).

[6] P. Tang, Q. Zhou, G. Xu, and S.-C. Zhang, Nat. Phys. **12**, 1100 (2016).

[7] C. Niu, H. Wang, N. Mao, B. Huang, Y. Mokrousov, and Y. Dai, Phys. Rev. Lett. **124**, 066401 (2020).

[8] X. Wan, A. M. Turner, A. Vishwanath, and S. Y. Savrasov, Phys. Rev. B **83**, 205101 (2011).

[9] G. Xu, H. Weng, Z. Wang, X. Dai, and Z. Fang, Phys. Rev. Lett. **107**, 186806 (2011).

[10] H. Yang, Y. Sun, Y. Zhang, W.-J. Shi, S. S. P. Parkin, and B. Yan, New J. Phys. **19**, 015008 (2017).

[11] Y. Xu, L. Elcoro, Z.-D. Song, B. J. Wieder, M. G. Vergniory, N. Regnault, Y. Chen, C. Felser, and B. A. Bernevig, Nature (London) **586**, 702 (2020).

[12] J. Zou, Z. He, and G. Xu, npj Comput. Mater. **5**, 96 (2019).

[13] P. Wadley, B. Howells, J. Železný, C. Andrews, V. Hills, R. P. Campion, V. Novák, K. Olejník, F. Maccherozzi, S. S. Dhesi, S. Y. Martin, T. Wagner, J. Wunderlich, F. Freimuth, Y. Mokrousov, J. Kuneš, J. S. Chauhan, M. J. Grzybowski, A. W. Rushforth, K. W. Edmonds et al., Science **351**, 587 (2016).

[14] L. Salemi, M. Berritta, A. K. Nandy, and P. M. Oppeneer, Nat. Commun. **10**, 5381 (2019).

[15] L. Šmejkal, J. Železný, J. Sinova, and T. Jungwirth, Phys. Rev. Lett. **118**, 106402 (2017).

[16] D.-F. Shao, G. Gurung, S.-H. Zhang, and E. Y. Tsymbal, Phys. Rev. Lett. **122**, 077203 (2019).

[17] S. M. Young and C. L. Kane, Phys. Rev. Lett. **115**, 126803 (2015).

[18] L. M. Schoop, M. N. Ali, C. Straßer, A. Topp, A. Varykhalov, D. Marchenko, V. Duppel, S. S. P. Parkin, B. V. Lotsch, and C. R. Ast, Nat. Commun. **7**, 11696 (2016).

[19] S. Klemenz, S. Lei, and L. M. Schoop, Annu. Rev. Mater. Res. **49**, 185 (2019).

[20] L. M. Schoop, A. Topp, J. Lippmann, F. Orlandi, L. Müchler, M. G. Vergniory, Y. Sun, A. W. Rost, V. Duppel, M. Krivenkov, S. Sheoran, P. Manuel, A. Varykhalov, B. Yan, R. K. Kremer, C. R. Ast, and B. V. Lotsch, Sci. Adv. **4**, eaar2317 (2018).

[21] M. M. Hosen, G. Dhakal, K. Dimitri, P. Maldonado, A. Aperis, F. Kabir, C. Sims, P. Riseborough, P. M. Oppeneer, D. Kaczorowski, T. Durakiewicz, and M. Neupane, Sci. Rep. **8**, 13283 (2018).

[22] A. Wang, I. Zaliznyak, W. Ren, L. Wu, D. Graf, V. O. Garlea, J. B. Warren, E. Bozin, Y. Zhu, and C. Petrovic, Phys. Rev. B **94**, 165161 (2016).

[23] R. Kealhofer, S. Jang, S. M. Griffin, C. John, K. A. Benavides, S. Doyle, T. Helm, P. J. W. Moll, J. B. Neaton, J. Y. Chan, J. D. Denlinger, and J. G. Analytis, Phys. Rev. B **97**, 045109 (2018).

[24] A. F. May, M. A. McGuire, and B. C. Sales, Phys. Rev. B **90**, 075109 (2014).

[25] C. Yi, S. Yang, M. Yang, L. Wang, Y. Matsushita, S. Miao, Y. Jiao, J. Cheng, Y. Li, K. Yamaura, Y. Shi, and J. Luo, Phys. Rev. B **96**, 205103 (2017).

[26] D.-F. Shao, S.-H. Zhang, G. Gurung, W. Yang, and E. Y. Tsymbal, Phys. Rev. Lett. **124**, 067203 (2020).

[27] A. S. Núñez, R. A. Duine, P. Haney, and A. H. MacDonald, Phys. Rev. B **73**, 214426 (2006).

[28] A. B. Shick, S. Khmelevskyi, O. N. Mryasov, J. Wunderlich, and T. Jungwirth, Phys. Rev. B **81**, 212409 (2010).

[29] H. Kontani, T. Tanaka, M. Naito, D. S. Hirashima, K. Yamada, and J. Inoue, J. Phys. Soc. Jpn. **77**, 275 (2008).

[30] R. Peters and Y. Yanase, Phys. Rev. B **97**, 115128 (2018).

[31] S. Lei, V. Duppel, J. M. Lippmann, J. Nuss, B. V. Lotsch, and L. M. Schoop, Adv. Quantum Technol. **2**, 1900045 (2019).

[32] A. Wang, S. Baranets, Y. Liu, X. Tong, E. Stavitski, J. Zhang, Y. Chai, W.-G. Yin, S. Bobev, and C. Petrovic, Phys. Rev. Res. **2**, 033462 (2020).

[33] P. Blaha, K. Schwarz, F. Tran, R. Laskowski, G. K. H. Madsen, and L. D. Marks, J. Chem. Phys. **152**, 074101 (2020).

[34] P. Giannozzi, S. Baroni, N. Bonini et al., J. Phys.: Condens. Matter **21**, 395502 (2009).

[35] J. P. Perdew, K. Burke, and M. Ernzerhof, Phys. Rev. Lett. **77**, 3865 (1996).

[36] M. D. Johannes and W. E. Pickett, Phys. Rev. B **72**, 195116 (2005).

[37] J. Kunes, W. Ku, and W. E. Pickett, J. Phys. Soc. Jpn. **74**, 1408 (2005).

[38] P. Larson and W. R. L. Lambrecht, J. Phys.: Condens. Matter **18**, 11333 (2006).

[39] S. Zhang, N. Aryal, K. Huang, K.-W. Chen, Y. Lai, D. Graf, T. Besara, T. Siegrist, E. Manousakis, and R. E. Baumbach, Phys. Rev. Mater. **1**, 044404 (2017).

[40] A. A. Mostofi, J. R. Yates, G. Pizzi, Y.-S. Lee, I. Souza, D. Vanderbilt, and N. Marzari, Comput. Phys. Commun. **185**, 2309 (2014).

[41] J. Qiao, J. Zhou, Z. Yuan, and W. Zhao, Phys. Rev. B **98**, 214402 (2018).

[42] W. Tremel and R. Hoffmann, J. Am. Chem. Soc. **109**, 124 (1987).

[43] S. Klemenz, L. Schoop, and J. Cano, Phys. Rev. B **101**, 165121 (2020).

[44] G. Hua, S. Nie, Z. Song, R. Yu, G. Xu, and K. Yao, Phys. Rev. B **98**, 201116(R) (2018).

[45] M. G. Vergniory, L. Elcoro, C. Felser, N. Regnault, B. A. Bernevig, and Z. Wang, Nature (London) **566**, 480 (2019).

[46] J. Sinova, S. O. Valenzuela, J. Wunderlich, C. H. Back, and T. Jungwirth, Rev. Mod. Phys. **87**, 1213 (2015).

[47] R. González-Hernández, L. Šmejkal, K. Výborný, Y. Yahagi, J. Sinova, T. c. v. Jungwirth, and J. Železný, Phys. Rev. Lett. **126**, 127701 (2021).

[48] H.-Y. Ma, M. Hu, N. Li, J. Liu, W. Yao, J.-F. Jia, and J. Liu, Nat. Commun. **12**, 2846 (2021).

[49] L. Šmejkal, R. González-Hernández, T. Jungwirth, and J. Sinova, Sci. Adv. **6**, eaaz8809 (2020).

[50] J. R. Schrieffer, J. Appl. Phys. **38**, 1143 (1967).

[51] Q. Wu, S. Zhang, H.-F. Song, M. Troyer, and A. A. Soluyanov, Comput. Phys. Commun. **224**, 405 (2018).